60 years of pss



High-Quality Plasmonic Materials TiN and ZnO:Al by Atomic Layer Deposition

Natalia Izyumskaya, Dhruv Fomra, Kai Ding, Hadis Morkoç, Nathaniel Kinsey, Ümit Özgür, and Vitaliy Avrutin*

Electromagnetic radiation when coupled to collective oscillations of free electrons, dubbed as plasmonics, makes it possible to manipulate light at dimensions well below the diffraction limit and substantially enhances light-matter interaction. Plasmonics has already enabled many novel technologies with a wide variety of application in chemical and biosensing, medical treatments, nonlinear and quantum optics, metamaterials, optical nanotweezers, nanolasers, solar cells, light-emitting diodes, and telecommunications. Coating the well-established semiconductor circuitry with metals, such as Au and Ag, imparts the stack with much coveted plasmonic properties, but the metals suffer from high dissipative losses, limited optical tunability, and poor mechanical, chemical, and thermal stabilities, which render them undesirable. Emerging alternative plasmonic materials, such as TiN and ZnO:Al, overcome these limitations and offer wide tunability of their electrical and optical properties. Among a wide range of techniques used for the preparation of TiN and ZnO:Al thin films, atomic layer deposition (ALD) offers advantages such as conformity, scalability, and low growth temperature, which makes this technique the most suitable for the integration of plasmonics with the complementary metal-oxide-semiconductor (CMOS) electronics. Herein, a brief review of recent advances in ALD-grown TiN and ZnO:Al thin films as pertained to plasmonic applications is given.

1. Introduction

The weak interaction between light and matter that represents the major hurdle in control and manipulation of photons has triggered a great interest in plasmonics in the past few decades. [1–6] Plasmonics relies on coupling photons into collective oscillations of free electrons on the surface of metals (surface plasmons), giving rise to surface-plasmon polaritons, electromagnetic waves propagating along metal/dielectric interfaces. The coupling of electromagnetic waves to the motion of free electrons enables confinement and control of light at scales much smaller than the diffraction limit through enhancing

Dr. N. Izyumskaya, D. Fomra, Dr. K. Ding, Dr. H. Morkoç, Dr. N. Kinsey, Dr. Ü. Özgür, Dr. V. Avrutin

Department of Electrical and Computer Engineering Virginia Commonwealth University

Virginia Commonwealth University Richmond, VA 23284, USA E-mail: vavrutin@vcu.edu

The ORCID identification number(s) for the author(s) of this article can be found under https://doi.org/10.1002/pssr.202100227.

DOI: 10.1002/pssr.202100227

light–matter interaction, as schematically shown in **Figure 1**. This makes possible to overcome the diffraction limit of conventional optics and localize electromagnetic waves on scales much shorter than the light wavelengths, paving the way to miniaturization of optical components.

Up to now, plasmonics has enabled the emergence of novel technologies with combined capabilities of photonics and microelectronics, and already a large variety of applications have been demonstrated, which include, but not limited to, chemical and biosensing, [7–9] medical treatments, [10,11] nonlinear and quantum optics,[12-14] metamaterials, [15,16] optical nanotweezers, [17] solar cells, [18,19] interconnects and modulators.[20,21] telecommunications (waveguides, nanoantennas, plasmonic filters, switches, routers, photodetectors),[22,23] light-emitting diodes, [24] and nanolasers. [25] Most common plasmonic materials are highly conductive metals (silver, gold, aluminum, etc.), among which gold and silver are the most popular.[7,26] The noble metals are featured with a high plasmonic figure of merit (FoM),

defined as the ratio of the real part of the permittivity to its imaginary part, FoM = $-\varepsilon'/\varepsilon''$, [27] but suffer from high inherent dissipative losses at optical frequencies.^[28] In addition, they exhibit very large, nontunable negative real permittivity in the near-infrared (NIR) and visible ranges, which is not beneficial for many important applications, such as epsilon-near-zero (ENZ) materials, hyperbolic metamaterials, optical modulators operating in the telecommunication wavelength range. Moreover, such drawbacks as low melting points, poor mechanical properties, limited tunability of their optical properties, tendency to oxidize under ambient conditions (in the case of silver), poor surface adhesion, formation of deep traps when diffusing into Si, make the incorporation of many traditional metals into microelectronics technology extremely challenging. This has spurred an intense search for robust alternative plasmonic materials compatible with the standard semiconductor fabrication, primarily, complimentary metaloxide-semiconductor (CMOS) technology. [28,29] A large variety of materials, including Si, Ge, III-V compounds, III-nitrides, transition metal nitrides, silicides, and germanides, transparent conducting oxides, perovskite oxides, and sulfides have been studied as alternative to gold and silver. [28,30,31] Reduced-dimension materials, including metal nanostructures, [7,32] graphene. [7,23,33-35] and



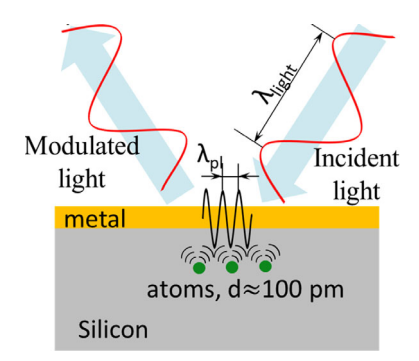


Figure 1. Electromagnetic wave couples into surface plasmon-polaritons that have wavelength $\lambda_{\rm pl}$ comparable with the size of atoms, $d_{\rm atom} \approx \lambda_{\rm pl} \ll \lambda_{\rm obston}$, thus enhancing the light-matter interaction.

phosphorene (single-monolayer phosphorus), [36] also have received considerable attention.

In this brief Review, we focus on atomic layer deposition (ALD) of two materials, titanium nitride (TiN) and Al-doped ZnO (AZO) that recently attracted a great deal of attention as plasmonic materials for visible and, primarily, NIR spectral regions. The focus on the ALD method is motivated by its excellent conformality, precise thickness control, and CMOS-compatible low deposition temperatures, as discussed in details in the following sections.

2. TiN Thin Films

Among the variety of the investigated materials, TiN stands out due to its gold-like optical properties and refractory nature. [29,37–40] Additional advantages of this material include tunability of its optical properties in the visible and NIR range, low-cost, high thermal and chemical stability, high melting point (2930 °C), high mechanical hardness, and bio- and CMOS compatibility. [30,31,41,42] **Figure 2**a,b shows the real and imaginary parts of the dielectric function of Au and sputtered TiN thin films, whereas Figure 2c compares recently published data on FoMs for TiN layers deposited by different techniques on various substrates. [37,43–47] For more published data on electrical and plasmonic properties of TiN films, see **Table 1**.

The high performance of TiN as a plasmonic material has been recently exploited for variety of applications, including plasmonic waveguides on sapphire, [48] nanohole metasurfaces on sapphire, [49] nanoantennas on sapphire, MgO and Si substrates, [37,50,51] and cancer treatment. [52] High-quality TiN is generally grown via reactive sputtering, [30,37,39,42,53,54] PLD, [43,55] molecular-beam epitaxy (MBE), [38,56] and ALD[41,51,57-68] techniques. Unfortunately, preparation of high-quality TiN usually requires high deposition or postdeposition annealing temperatures that are not compatible with CMOS processes. Nevertheless, a peak plasmonic FoM of $\approx\!4.5$ has been demonstrated for TiN films deposited on a bulk MgO substrate by reactive sputtering at a substrate temperature of 650 °C. [37] The MBE method allows for substantial improvement of material quality that results in low optical loss. The ϵ'' value as low as 10 was

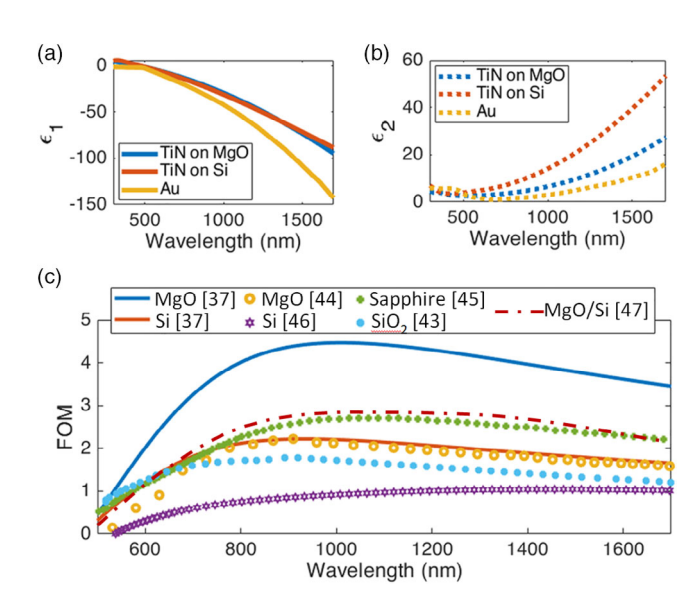


Figure 2. a) Real and b) imaginary parts of the permittivity of Au and TiN thin films deposited by sputtering onto (100)Si and (100)MgO substrates at temperatures of 700 and 650 °C, respectively. c) FoM for TiN films deposited on various substrates (MgO, sapphire, Si, SiO₂, and MgO/Si stack) by sputtering,^{137,44–46} pulsed laser deposition (PLD),^[43] and ALD.^[47] a–c) Adapted with permission.^[37] Copyright 2019, American Chemical Society.

obtained by Maurya et al.^[56] for TiN films grown on sapphire by plasma-assisted MBE at 600 °C. Using very high substrate temperature of 1000 °C during MBE growth allowed Guo et al.^[38] to achieve single-crystalline, stoichiometric, highly metallic TiN films with an electron concentration of 9.2×10^{22} cm⁻³ and low optical loss ($\varepsilon''=18$) due to improved structural quality that resulted in a peak plasmonic FoM as high as ≈ 5.8 (see Table 1). However, these temperatures are too high for the CMOS industry, which requires a relatively low ceiling temperatures about 550 °C. In addition, the growth of stoichiometric TiN films by sputtering or chemical vapor deposition (CVD) is rather challenging because titanium is highly reactive and easily forms titanium oxynitride as a result of reaction with residual gases.^[38]

Being a low-temperature technique, ALD appears to be the most suitable for deposition of nitride and oxide films for plasmonic applications, as it is a CMOS-compatible scalable method which provides low-temperature, conformal, and pin-hole free deposition with subnanometer thickness control. However, relatively high concentration of defects in ALD materials associated with low process temperature compared with such methods as MBE, sputtering, or PLD as well as relatively large level of oxygen and carbon contaminations give rise to a high optical loss in the ALD-deposited TiN. Thus, the attainment of CMOScompatible TiN comes at the expense of trade-off between sufficiently low deposition temperature and optical loss. Nevertheless, the typical ALD process temperatures (200-300 °C) are well below the upper limit of the CMOS technology (\approx 550 °C). Therefore, there is a room to improve the structural quality of ALD TiN by increasing the deposition temperature toward 450-500 °C and reducing the level of contaminations via careful optimizations of process parameters and choice of





Table 1. Deposition technique, deposition temperature T_S , thickness t, resistivity ρ , the real (ε') and the imaginary (ε'') parts of the dielectric permittivity, and plasmonic FoM for TiN films deposited on various substrates.

Film/substrate	Method ^{a)}	$T_S [^{\circ}C]^{a)}$	t [nm]	$ ho~[\Omega~{ m cm}]$	arepsilon' at 1550 nm	arepsilon'' at 1550 nm	FOM at 1550 nm	Ref.
TiN/Si	PE-ALD	450	100	-	-62	31	2.0 (peak 2.4 at \approx 1000 nm)	[47]
TiN/MgO/Si		450	100	_	-60	24	2.5 (peak 2.8 at \approx 1250 nm)	
Ti/MgO		450	100	_	-63	24	2.6 (2.9 peak at \approx 1270 nm)	
TiN/sapphire	PE-ALD	450	85	3.1×10^{-5}	-63	27	2.33 (peak 2.8 at \approx 1200 nm)	[57]
TiN/Si	PE-ALD	250	90	_	-22	43	0.5	[51]
TiN/SiO ₂		250	90	_	-24	41	0.6	
TiN/MgO		250	90	_	-30	26	1.2	
TiN/SiO ₂ /Si	PE-ALD	300	27	34.1×10^{-5}	-7	39	0.18 (peak 0.54 at 900 nm)	[59]
		300	216	$34.1 \times \mathbf{10^{-5}}$	-27	35	0.77 (peak \approx 1 at 900 nm)	
TiN/SiO ₂ /Si	ALD	350	10	${\approx}17\times10^{-5}$	-28	66	0.4	
TiN/SiO ₂ /Si	PE-ALD	300	30	5.3×10^{-5}	_	_	_	[62]
TiN/MgO	PE-ALD	300	57	2.9×10^{-5}	_	_	_	[73]
TiN/sapphire		300	57	5.0 × 10	_	_	_	
TiN/SiO ₂ /Si		300	57	6.7 × 10	=	=	=	
TiN/MgO	PE-ALD	300 + annealing at 650	57	2.0×10^{-5}	_	_	=	[73]
TiN/sapphire			57	4.5 × 10	_	_	_	
TiN/SiO ₂ /Si			57	5.5 × 10	_	_	_	
TiN/SiO ₂ /Si	PE-ALD	300–350	25-40	6.0×10^{-5}	=	=	=	[66]
TiN/Si	PE-ALD	250	34	8.6×10^{-5}	_	_	_	[61]
TiN/sapphire	MBE	1000	100	3.4×10^{-5}	-83	18	4.6 (peak ≈5.8 at ≈1150 nm)	[38]
TiN/MgO	MBE	600	80	_	-68	19	3.6	[56]
TiN/sapphire		600	80	_	-50	10	5	
TiN/SiO ₂ /Si	PLD	RT	_	_	-80	60	\approx 1.3 (peak \approx 1.8 at 920 nm)	[43]
TiN/sapphire	PLD	780	130	_	_	_	Peak 1.9 at ≈870 nm	[55]
TiN/MgO		780	130	5.3×10^{-5}	_	_	Peak 1.7 at ≈900 nm	
TiN/Si	PLD	600–700		1.5×10^{-5}	_	_	_	[72]
TiN/Si	Reactive RF MS	700	80	_	-78	43	1.8 (peak 2.2 at ≈900 nm)	[37]
TiN/MgO		650	80	_	-75	20	3.7 (peak 4.5 at 1000 nm)	
TiN/sapphire	DC MS	850	30	_	-61	26	2.3 (peak ≈2.7 at 1100 nm)	[45]
		850	200	_	-62	21	2.9 (peak ≈3.3 at 1150 nm)	
TiN/Si	Reactive MS	600	41	_	-24	24	1	[46]
TiN/sapphire		600	39	29×10^{-5}	-7	23	0.3	
TiN/MgO		600	29	6.5×10^{-5}	-53	36	1.5	
TiN/sapphire	Reactive DC MS	800	30–50	_	-16	19	0.84	[30]
TiN/sapphire	Reactive DC MS	500	30	_	-17	10	1.7	[39]
TiN/MgO	Reactive DC MS	800	10	_	-66	22	3	[53]
TiN/MgO	Reactive DC MS	600	≈35	_	-70	26	2.7	[54]
TiN/Si	Reactive RF MS	RT	50	_	-55	49	1.12 (peak ≈1.5 at ≈900 nm)	[71]

^{a)}The following abbreviations are used in the table: plasma-enhanced atomic layer deposition (PE-ALD), pulsed laser deposition (PLD), molecular-beam epitaxy (MBE), radio frequency (RF), direct current (DC), magnetron sputtering (MS), room temperature (RT).



Ti precursors and system hardware materials. These efforts are discussed in detail below.

Plasma-enhanced ALD (PE-ALD)^[69] widely used for TiN fabrication allows deposition either at even lower temperatures or improvement of the material crystallinity without substantial increase in the process temperature due to plasma-enhanced reactivity of precursors. Optical and electrical properties of the films can be easily tuned by varying ALD conditions and/or postgrown treatments. In case of TiN, ALD typically offers low, highly controllable growth rates of 0.1–0.5 nm per cycle. A wide variety of precursors, including tetrakis(dimethylamino)titanium (TDMAT), tetrakis(diethylamino)titanium (TDEAT), and titanium tetrachloride (TiCl₄) are used for the ALD growth of TiN, with TDMAT being the most popular one. It has a moderate decomposition temperature and a large ALD-window temperature range, enabling wide tunability of TiN optical properties. The ALD window is the temperature range within which self-limiting growth mechanism is operative (see Figure 3b). At temperatures below the ALD window, the precursor could condense on the substrate surface, leading to ineffective purging and resulting in an increased growth rate and poor material quality (Figure 3b). On the other hand, surface reactions could remain incomplete because of low temperature, which would result in a decreased growth rate. On the high-temperature end of the ALD window, decomposition of the metalorganic precursor could lead to a CVD-type growth with increased growth rate, or enhanced desorption of the precursor may decrease the growth rate. Temperatures both above and below the ALD give rise to deviation from stoichiometry of resultant material, degrading its plasmonic FoM.

Briggs et al.^[51] used PE-ALD of TiN to fabricate CMOS-compatible plasmonic nanoantennas. TiN layers were grown

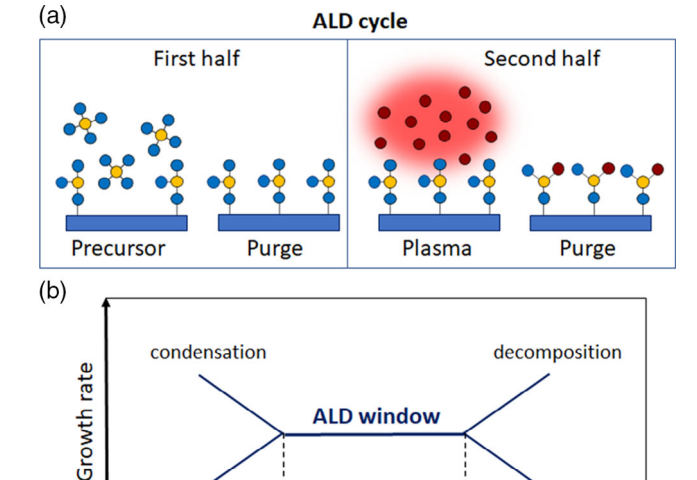


Figure 3. a) Schematic illustration of a typical PE-ALD cycle. During the first half-cycle, a pulse of precursor molecules chemisorbing on a heated surface is followed by a purge step to remove excess precursor species. During the second half-cycle, the chemisorbed precursor is exposed to plasma which provides the activation energy for the formation of a desired material. b) Schematic showing the ALD temperature window.

Substrate temperature

incomplete

on Si, SiO2, and MgO substrates at 250 $^{\circ}\text{C}$ using TDMAT as precursor with a plasma exposure time that varied from 20 to 110 s. It was found that longer plasma exposure times are favorable for reducing carbon and oxygen contaminations, which are likely responsible for the increased absorption in the NIR range. Xray photoelectron spectroscopy (XPS) revealed that the TiN layers deposited with a plasma exposure time of 20 s contained 13% oxygen and 7% carbon, whereas the films grown with 80 s plasma exposure time had only 3% oxygen and 4% carbon. As a result, the layers grown at longer plasma exposure times showed improved optical properties (more negative real part of the permittivity and lower loss). Annealing of the ALD TiN films on Si in vacuum for 2h was found to further improve the optical properties of TiN. As annealing temperature increased from 250 to 650 °C, the real of permittivity became more negative, the imaginary part decreased, and the screened plasma frequency at which the real permittivity changes from positive to negative, indicating the onset of metallic behavior, increased. Using the optimized plasma exposure times and postdeposition anneals, Briggs et al. [51] have achieved a plasma frequency of ≈622 nm. Although a temperature of 650 °C is too high for the CMOS technology, annealing at temperatures below 500 °C are acceptable for CMOS, and even as-grown TiN layers shows plasma frequency values in the visible range, proving that the ALD grown TiN is certainly suitable for plasmonic applications in the visible and NIR ranges.

Fomra et al.^[57] have reported high plasmonic quality TiN films grown by PE-ALD on c-plane sapphire. TiN layers with low losses, high metallicity, and a plasma frequency below 500 nm were achieved at substrate temperatures less than 500 °C by optimizing the ALD parameters (chemisorption time, plasma exposure time, and substrate temperature). It was found that a reduction in chemisorption time from 2 to 0.5 s mitigated premature decomposition of the TDMAT precursor at substrate temperatures above 375 °C (TDMAT decomposes rapidly at temperatures around 450 °C^[70]). In concert with the findings by Briggs et al., [51] a longer plasma exposure time was found to reduce impurity concentration in the TiN films, especially in the layers grown at higher temperatures. Figure 4a shows the carbon and oxygen concentrations in the films grown at 450 °C as a function of plasma exposure time $t_{\rm plasma}$. One can see that the impurity concentrations drop abruptly as $t_{
m plasma}$ increases from 15 to 25 s and then virtually saturate as $t_{\rm plasma}$ increases further to 35 s. This effect was particularly noticeable at temperatures around 450 °C because the samples deposited at higher temperatures were more contaminated with oxygen and carbon compared with the samples deposited at lower temperatures, as revealed by XPS examination. For example, the TiN films deposited at 375 °C with $t_{\rm plasma} = 10 \, \rm s$ exhibited less than $2 \pm 0.5\%$ carbon and oxygen impurities, whereas 4% carbon and 3% oxygen were detected in the films grown at 450 °C. This finding was explained by premature decomposition of the precursor on the substrate surface at 450 °C, wherein the Ti species readily bonded to impurities from the environment. From this point of view, precursors stable at higher temperatures, such as TDEAT, could result in films with better optical quality.

The extended plasma exposure time was also found to improve optical performance of the material by facilitating the complete conversion of Ti into stoichiometric TiN.^[57] As shown in

desorption





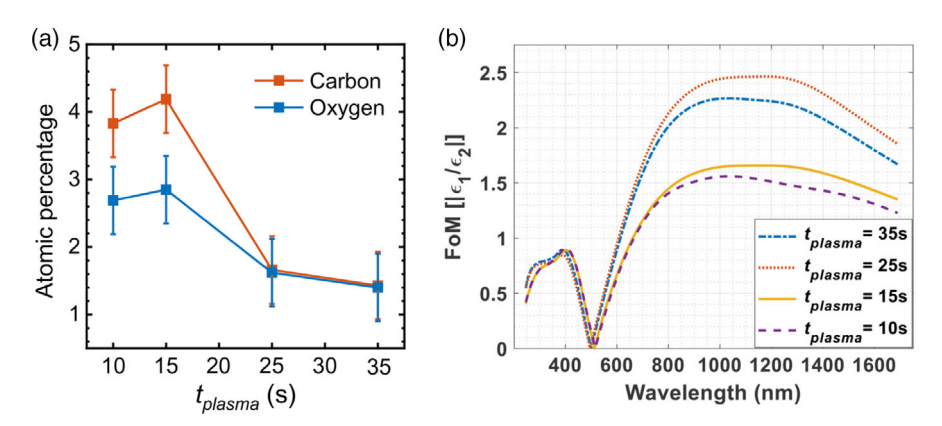


Figure 4. a) Concentration of carbon and oxygen in the TiN films grown on sapphire by PE-ALD at 450 °C as a function of plasma exposure time, $t_{\rm plasma}$. b) FoM of the TiN films grown at a substrate temperature of 450 °C with different plasma exposure times. a,b) Reproduced with permission. Copyright 2020, AIP Publishing.

Figure 4b, FoM of the TiN layers grown at 450 °C increases as the plasma exposure time rises from 10 to 25 s, however, drops slightly at a plasma exposure time of 35 s. X-ray diffraction (XRD) studies revealed that this drop can be explained by a reduced structural quality of the films deposited with long plasma exposures due to plasma damage. Therefore, an optimized trade-off between reduced impurity concentration and increased defect density with plasma exposure time resulted in the best optical properties of the TiN layers grown with $t_{\rm plasma}=25~{\rm s}$ (Figure 4b).

The permittivity of the optically thin films is affected by the substrate and the nonideal layer near the substrate/TiN interface. Therefore, FoM is expected to be dependent of the layer thickness. Fomra et al. [57] studied thickness dependence of the optical performance of the ALD-grown TiN layers. As shown in Figure 5a, the peak FoM value rises from 2.2 to 2.8 as the film thickness increases from 30 to 80 nm, then tends to saturate. The observed dependence is due to the contribution from the lower quality layer near the substrate/TiN interface. Beyond a few skin depths ($\delta \approx 15 \text{ nm}$ at the frequency corresponding to the peak FoM), this contribution becomes negligible. Figure 5b shows the substrate temperature dependence of the peak FoM measured for optically thick films (≈100 nm). As shown in Figure 5b, 450 °C is the optimal deposition temperature, which also produces the lowest film resistivity of $31 \,\mu\Omega$ cm.^[57] It is interesting that a sharp drop in FoM at substrate temperatures above 450 °C is accompanied by a rapid increase in growth rate, from $1.3 \,\text{Å}\,\text{cycle}^{-1}$ at $450 \,^{\circ}\text{C}$ to $4.2 \,\text{Å}\,\text{cycle}^{-1}$ at $500 \,^{\circ}\text{C}$. Such increase in the deposition rate is indicative of CVD-like growth mode at high temperatures caused by premature decomposition of TDMAT on the substrate surface and formation of Ti-reach material, which is obviously not favorable for optical performance of TiN. Figure 5d shows the FoM for the 85 nm-thick TiN layer grown at the optimized conditions (a substrate temperature of 450 °C, a chemisorption time of 0.5 s, and a plasma exposure time of 25 s). A thorough optimization of the growth parameters allowed Fomra et al.^[57] to achieve TiN layers exhibiting a high plasmonic FoM of 2.8.

It should be emphasized that the growth of high-purity TiN by the low-temperature PE-ALD is rather challenging. Carbon and $\,$

oxygen are the most common impurities in the ALD-grown film. Carbon comes from precursors. Unfortunately, N₂ or NH₃ plasma used for the nitride growth removes carbon contaminations from the substrate surfaces less efficiently as compared with oxygen plasma. Oxygen species come from the residual gas in the growth chamber, chamber walls contaminated during previous oxide growths, process and purge gases, and precursors.^[59,61,69] As titanium has a high affinity for oxygen, even minor oxygen contamination in an ALD chamber results in titanium oxidation during the growth, which is a serious complication of the ALD technique. In worst cases, background oxygen can lead to titanium oxynitride growth. ^[60]

Otto et al.[59] deposited TiN layers on SiO2 substrates by conventional PE-ALD with TDMAT precursor at a substrate temperature of 300 °C. In that work, a mixed hydrogen+nitrogen plasma was used, where hydrogen radicals helped to remove [(CH₃)₂ N] ligands from the metal-organic precursor, and nitrogen radicals bonded to open titanium sites. Using in situ spectroscopic ellipsometry, Otto et al. [59] studied the evolution of TiN properties throughout the film growth. The real part of the permittivity showed the strongest thickness dependence, with substantial improvement as the film thickness increased to 216 nm. This enhancement was attributed to increased carrier concentration and mobility as a result of the cumulative plasma time exposure of the growing film. The imaginary part of the permittivity showed moderate gradual decrease with increasing film thickness. The FoM calculated from the ellipsometry data revealed that even the thin films (<10 nm) were plasmonic, and the FoM increasing with the film thickness, reaching ≈ 1 at \approx 900 nm wavelength. Otto et al. [59] emphasized that the properties of the ALD-grown TiN layers were very sensitive to oxygen cross-contamination in the ALD chamber resulting from previously performed depositions of metal oxides, such as AlOx, SiOx, TiO_x , HfO_x , CoO_x , WoO_x , and MoO_x . Auger electron spectroscopy (AES) revealed increased oxygen concentrations in the TiN films grown in the chamber seasoned with previous oxide depositions as compared with the layers deposited in the cleaned chamber. Due to increased oxygen contamination, the TiN layers grown in the seasoned chamber showed inferior FoMs, sheet



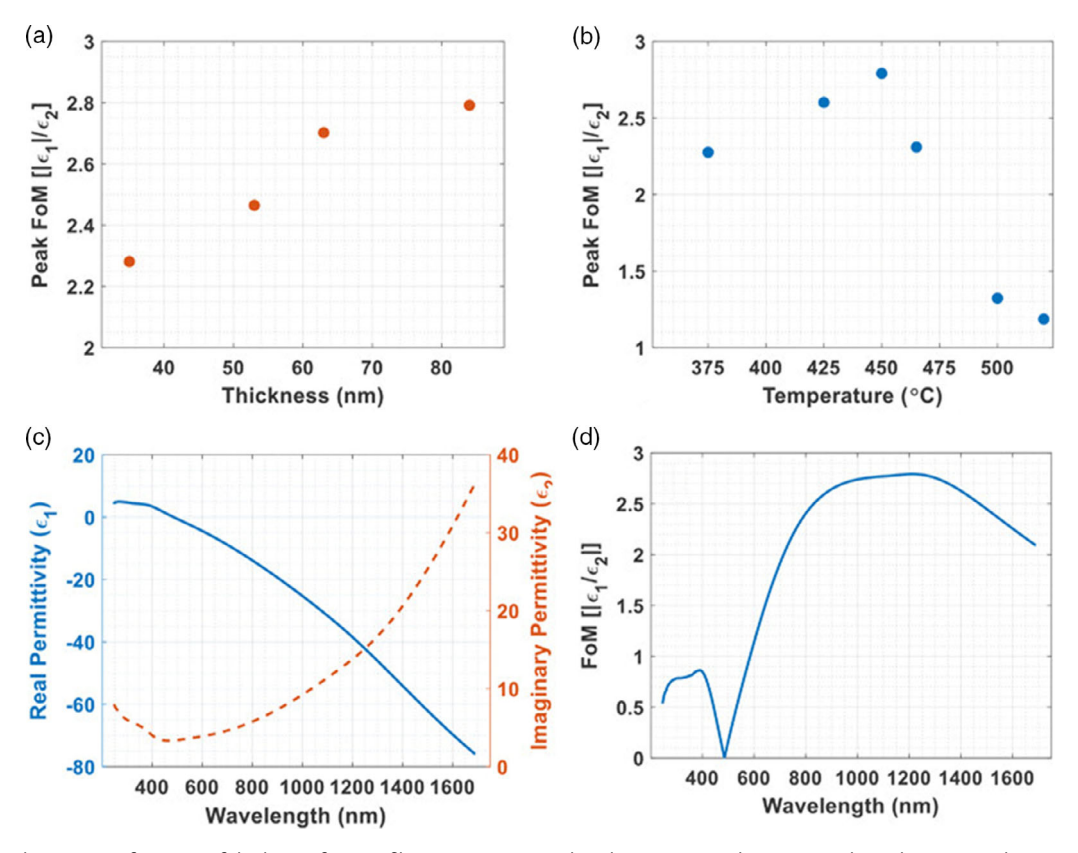


Figure 5. a) Peak FoM as a function of thickness for TiN films grown on sapphire by PE-ALD under optimized conditions (a substrate temperature of 450 °C, a chemisorption time of 0.5 s, and a plasma exposure time of 25 s). b) Peak FoM as a function of a substrate temperature for optically thick TiN films. c) Real and imaginary parts of the permittivity and d) FoM (peaking at 2.8) for the film grown under the optimized conditions. a–d) Reproduced with permission. [57] Copyright 2020, AIP Publishing.

resistance, and increased resistivity (from 341 to 547 $\mu\Omega$ cm for films grown in the clean and seasoned chamber, respectively).

Rayner et al. [61] investigated various sources of oxygen species in a typical PE-ALD reactor and identified six sources: system leaks, process gases (Ar, N2, and H2), elastomer permeation, process pump back diffusion, outgassing of water adsorbed on reactor surfaces, and plasma etching of the silica plasma tube. Process gases have been found to be the primary source of oxygen contamination, 99.999% purity grade process gases contain up to ppm levels of oxygen impurities, including O2, water, CO, and CO₂. To achieve ultrahigh purity conditions in the ALD reactor, Rayner et al. [61] addressed all of the aforementioned sources of oxygen contaminations, except of plasma etching of the silica tube. The PE-ALD deposition of TiN films on SiO₂/Si substrates was carried out using TiCl₄ and TDMAT precursors at 350 °C and 250 °C, respectively. In both cases, TiN layers with oxygen content below 1 at% were obtained. The authors point out that further improvement in TiN purity can be achieved by replacing the silica plasma tube with sapphire one. Indeed, it has been reported^[62] that the sapphire-based inductively coupled plasma (ICP) source enables lower oxygen contamination of TiN layers as compared with the quartz source. Other advantages of the sapphire source include higher deposition rates, better crystallinity, and lower film resistivity. [62] Krylov et al. [62] also reported that the increase in the reactive gas flow resulted in higher oxygen contamination for both ICP source materials and that the oxygen concentration in the films depended on the reactive gas nature (N2, NH3, or H2). The lowest oxygen concentration ($\approx\!1\%$) was observed for TiN grown with the sapphire plasma source at a low flow of hydrogen plasma, whereas the films deposited with the use of quartz plasma source at a high hydrogen flow suffered from the highest oxygen contamination ($\approx\!45\%$). The layers grown with the sapphire plasma source at a low H2 flow also showed the lowest resistivity ($\approx\!53\,\mu\Omega$ cm for 30 nm-thick films) apparently due to the lowest oxygen contamination level. It is interesting to note that so grown films had a significant carbon content ($\approx\!8\%$). However, the carbon contamination did not degrade the film conductivity, as TiC itself is conductive.

Realizing the potential of TiN-based plasmonics through integration with the CMOS-based electronics necessitates the growth of high-quality TiN layers on Si substrates under CMOS-compatible conditions, namely the growth temperatures. It has been well established that structural performance and physical properties of thin films depend drastically on the substrates used. Unfortunately, Si is a poor substrate choice for epitaxial growth of TiN due to the large lattice mismatch between Si and TiN (21.9%). Up to the time of this writing, only moderate plasmonic properties have been achieved for TiN films grown on Si substrates using various deposition methods such as sputtering, [37,54,71] PLD, [72] and ALD [51] (see Figure 2). A low

resistivity of 15 $\mu\Omega$ cm has been achieved by PLD at temperatures as high as 700 °C. [72] As for low-temperature growth, TiN films grown by ALD on Si at 250 °C exhibited weak metallic character and much higher losses at the telecommunication wavelength of 1550 nm as compared with TiN films on MgO (see Table 1), although the TiN/Si films were used to demonstrate fully CMOS-compatible plasmonic nanoantennas.^[51] Due to the close in-plane lattice constants of MgO (4.213 Å) and TiN (4.241 Å). MgO substrate promote epitaxial growth and ensure high structural quality, good optical properties, low loss, and low electrical conductivity. Studying a large variety of amorphous, polycrystalline, and single-crystalline substrates, Krylov et al.^[73] have found that TiN grown by ALD on single-crystal bulk MgO substrates at 300 °C showed the lowest resistivity (\approx 20 $\mu\Omega$ cm). This value is very close to that for TiN deposited for PLD at much higher temperature of 700 $^{\circ}\text{C.}^{[72]}$

Very recently, Ding et al. [47,74] addressed the insufficient optical quality of TiN films on Si substrates by inserting a thin (10 nm) MgO interlayer. The MgO layers were grown on Si (001) substrates by plasma-assisted MBE at 680 °C. TiN layers \approx 100 nm thick were then grown on the MgO/Si (001) templates by PE-ALD at a moderate substrate temperature of 450 °C using TDMAT and nitrogen plasma as the Ti and N precursors, respectively. For comparison purposes, TiN layers were grown in the same run directly on Si (001) without an MgO interlayer and on bulk MgO (001) substrates. As shown in Figure 6a, the MgO interlayer enhanced the plasmonic FoM at the telecommunication wavelength of 1550 nm from 2.0 for TiN/Si to 2.5 for TiN/MgO/Si, while the peak FoM (at ≈1300 nm) increased from 2.4 to 2.8, respectively. These values were comparable with those associated with the films grown on bulk MgO (001) substrates. XRD measurements revealed that TiN grew on the MgO/Si templates epitaxially, with an epitaxial relationship of TiN (001) || Si (001) and TiN [110] || Si [110]. The interesting finding was that even moderate structural quality MgO interlayer gave rise to a dramatic improvement in TiN structural perfection and thus optical quality. Scanning transmission electron microscopy (STEM) study of sample cross-sections, supported by the reflection high energy electron diffraction (RHEED) observations of the growth evolution, indicated that the MgO

interlayer commenced in the amorphous state due to the large lattice mismatch between Si and MgO and a low substrate temperature of 300 °C used for MgO layer nucleation. As the MBE growth proceeded at 680 °C, textured polycrystalline MgO with (001) preferred orientation emerged. The intermediate MgTiO or MgTiON sublayer, as evidenced by X-ray energy dispersive spectroscopy (EDX), was formed by intermixing between the MgO and TiN layers during the ALD growth procedure. As a result, the MgO interlayer was composed of a 3 nm amorphous MgO sublayer at the Si/MgO interface, a 6 nm polycrystalline MgO sublayer, and a 2 nm-thick MgTiO or MgTiON sublayer at the MgO/TiN interface. However, the MgTiO or MgTiON sublayer did not exhibit the spinel structure characteristic of Mg-containing complex oxides likely due to the relatively low ALD growth temperature. Inheriting from the polycrystalline MgO, the TiN film initialized in the realm of a competition between different growth orientations for the first 20 nm. As the growth proceeded, thermodynamically favorable (001)-oriented TiN grains began to prevail and finally won the competition against other grain orientations due to the lowest surface energy of the TiN (001) plane.^[75] It should be stressed that the MgO interlayer should not necessarily be grown by MBE, the thin MgO interlayer may be successfully deposited by low-temperature ALD, providing comparable crystalline quality and maintaining the CMOS process compatibility.^[76]

Figure 6b shows the real and imaginary parts of the permittivity for the ALD-grown TiN layers on the MgO/Si template as well as on Si and bulk MgO substrates. One can see that the real part of the permittivity turns out to be virtually independent of the substrate material. In general, higher crystalline quality should provide higher metallicity (more negative ε') in TiN films. However, such factors as stoichiometry and oxygen contamination could have more significant effect on metallicity. [54,59] Therefore, TiN films with better crystal quality had not always exhibited higher metallicity. As noted, the TiN films in this work were grown under the same PE-ALD conditions, so similar metallicity was attributed to similar stoichiometry and oxygen impurity concentration among the samples grown on different substrates. In contrast, the optical losses for TiN on MgO/Si were significantly lower as compared with those for TiN on Si due to the improvement in crystallinity

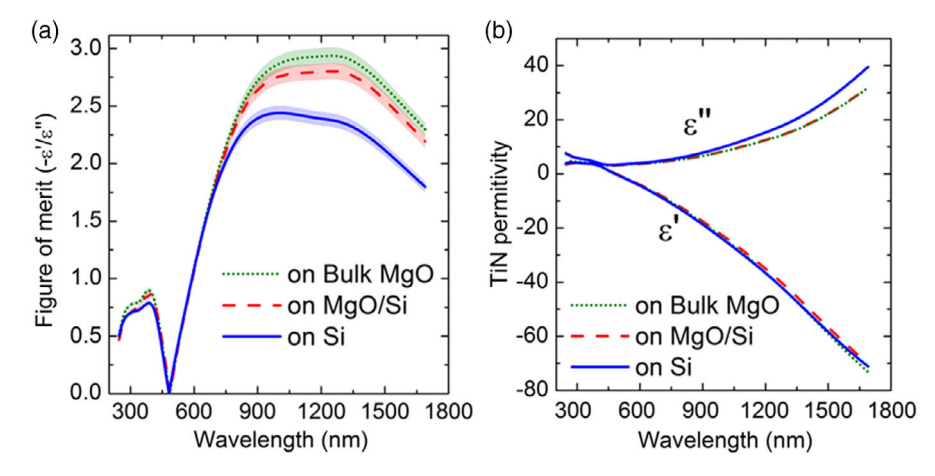


Figure 6. a) FoM and b) real and imaginary parts of the permittivity for TiN thin films grown on Si (001), Si (001)/MgO, and bulk MgO (001) substrates as a function of wavelength. The shadowed regions in (a) represent experimental error. a,b) Adapted under the terms of the CC-BY Creative Commons Attribution 4.0 International license (https://creativecommons.org/licenses/by/4.0). [47] Copyright 2021, The Authors, published by Wiley-VCH.



via the insertion of the MgO interlayer, and were comparable with those in the films grown on bulk MgO (Figure 6b). TiN grown on bulk MgO showed the highest FoMs (Figure 6a), which is consistent with the fact that bulk MgO possesses much better lattice matching to TiN than Si and higher crystal quality compared with the MgO interlayer. The FoM values for the films grown on the MgO/Si templates are only slightly lower than that for TiN on bulk MgO, but considerably improved as compared with those of TiN on Si. The TiN films grown on the MgO/Si templates exhibit the best performance among films grown on Si by PE-ALD^[51] and reactive sputtering^[54,71] at CMOS-compatible temperatures, and even at higher than 600 °C,^[37] whereas also achieving their peak and fairly consistent performance in the telecommunications range.

To evaluate the device potential of the PE-ALD-deposited TiN, Fomra et al.^[77] designed, fabricated, and characterized mechanically robust metasurfaces exhibiting plasmonic colors across the visible and the NIR spectrum. Such metasurfaces are attractive for security holograms invisible to eye. Using e-beam lithography and dry etching, Fomra et al. [77] fabricated circular subwavelength apertures (nanoholes) in 41 nm-thick TiN layers grown by PE-ALD on sapphire substrates under optimized conditions. The nanoholes with radii varying from 75 to 150 nm were arranged in a hexagonal pattern, as shown in Figure 7a. These patterned films exhibit polarization-independent and angle insensitive (±10°) extraordinary transmission (EOT)[78] in the visible and the short-wave IR spectral regions (550–1040 nm), which is accessible by conventional Si CCD detectors. Figure 7b shows the simulated (using Comsol Multiphysics software) and experimentally measured transmission spectra of a representative structure with a separation between the nanoholes of 200 nm and a hole radius of 150 nm. The EOT peak at \approx 1050 nm is caused by the formation of plasmonic Bloch modes on the surface of the TiN/air interface due to the interference of propagating surface plasmons, as observed in patterned thin metallic films.^[78–80] In brief, the effect is based on coupling the incoming electromagnetic waves to the propagating surface plasmon modes on the internal surfaces of the circular nanoholes, due to the momentum imparted by the periodic structure. These surface plasmons, launched from the edge of each nanohole, interfere to form plasmonic Bloch modes which result in a band structure. [79] As shown in Figure 7b, the

spectral position of the peak, along with the efficiency of transmittance, match well with the simulations. This is indicative of sufficiently high structural quality of TiN epitaxially grown on c-plane sapphire that enables a smooth sidewall profile, unlike gold and silver which exhibit rough edges due to grain formation. Figure 7c compares the simulated (COMSOL Multiphysics) responses of similar structures based on gold and silver films with a 4 nm Cr adhesion layer, which are required to provide continuous films. Despite the simulated response from the TiN metasurface appearing somewhat worse compared with the ideal metal metasurfaces, the side-wall roughness inherent to the polycrystalline nature of metal films would lead to higher scattering/radiation losses, further limiting their performance. [81] Figure 7d shows the color palette for EOT achievable by varying the periodicity and radii of the nanohole array. The EOT transmission peak is continuously tunable between 750 and 1040 nm. To reiterate, as the spectral response of all the designed metasurfaces can be easily imaged using inexpensive silicon-based photodetector arrays, these structures exhibiting plasmonic colors can be utilized to design covert security features, using arrays of patterns that have similar appearances in the visible spectrum but a different spectral signature in the short-wave IR region.

3. ZnO:Al Thin Films

Another class of alternative plasmonic materials is transparent conducting oxides (TCOs) such as aluminum zinc oxide (AZO), gallium zinc oxide (GZO), and indium tin oxide (ITO). Being CMOS-compatible materials with low optical losses, tunable optical properties, metal-like conductivity, and wellfabrication processes, TCOs have found established applications in plasmonics, metamaterials, and nonlinear optics. [26,28–30,42,82,83] Due to the real part of the permittivity approaching zero at telecommunication wavelengths (1260-1625 nm) as well as small losses in this range, TCOs are considered as promising ENZ materials.^[28] Among the TCOs, AZO and GZO are particularly attractive, as ZnO is a well-studied material composed of nontoxic and naturally abundant elements. This material tolerates high levels of doping that gives rise to high conductivity.^[84] At the telecommunication wavelength of 1550 nm,

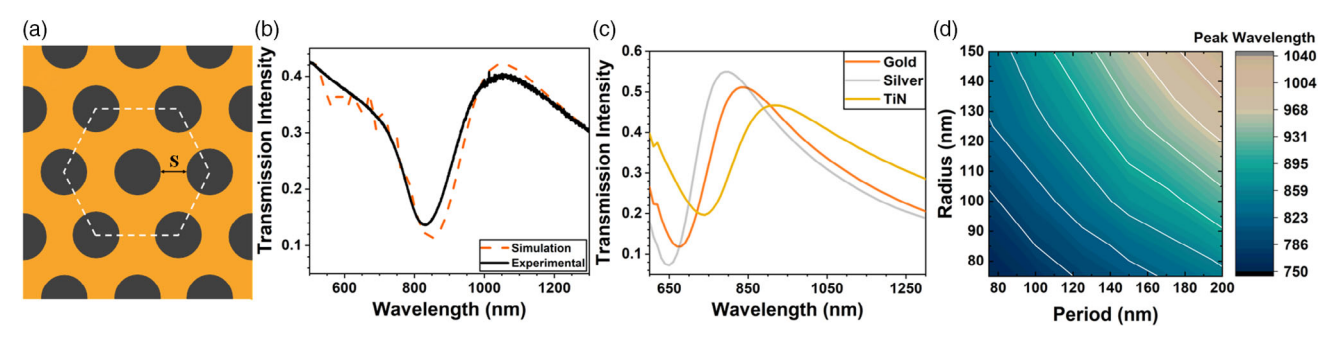


Figure 7. a) Schematic of the hexagonal array metasurface. S stands for separation. b) Simulated (dashed) and measured (solid) transmission spectra of a metasurface with separation of 200 nm and radius of 150 nm. The kinks on the measured spectrum at wavelengths below 650 nm are due to diffraction effects, whereas the smooth peak around 1050 nm is due to EOT. c) Simulated transmission spectra for Au-, Ag-, and TiN-based metasurfaces with radius of 125 nm and separation of 150 nm. Simulations for Au and Ag metasurfaces are carried out assuming the presence of a 4 nm-thick Cr adhesion layer. d) EOT peak positions as a function of the radius and period. EOT peaks cover the wavelength range from 750 to 1040 nm. a–d) Adapted with permission.^[77] Copyright 2021, Optical Society of America.





losses in AZO are more than three times lower than losses in silver, whereas GZO exhibit slightly inferior characteristics. ^[29] The Al- and Ga-doped ZnO layers can be deposited by a variety of techniques, including sputtering, ^[42,85,86] MBE, ^[87–89] PLD, ^[83,90,91] CVD, ^[92,93] and ALD. ^[94–103] Typically, AZO films are grown by ALD at substrate temperatures not higher than 250 °C with the use of diethylzinc (DEZ), trimethylaluminium (TMA), and water as Zn, Al, and oxygen precursors, respectively. ^[95,97–99,102] The decomposition of water molecules results in the absorption of OH $^-$ radicals on the surface, which act as active sites for Zn $^+$ and Al $^+$ ions.

As AZO is not a stoichiometric compound, its physical properties are drastically dependent on deposition conditions. Indeed, along with Al content of AZO, the ENZ wavelength can be tuned by adjusting deposition temperature, film thickness, postdeposition thermal treatment, [95-97,99] and even by adding ZnO buffer layers and protecting layers (e.g., HfO₂ or Al₂O₃) preventing Zn evaporation upon high-temperature treatment. [101] Up to date, several groups reported on the tuning of ENZ wavelength in the ranges 1320–2300, [94] 1450–1545, [101] 1500–1700, [95] 1550– 1700, [96] 1600–2200, [99] and 1800–2400 nm. [97] As an example, Figure 8 shows ENZ wavelength dependences on substrate temperature, dopant concentration, and thickness for AZO layers grown by ALD on silica and silicon substrates by Gurung et al. [96] The ENZ wavelength blueshifts as the substrate temperature increases from 225 to 250 °C (Figure 8a,d), which can be explained by the increase in doping efficiency (the ratio of electrically active Al species to total Al content in the matrix) as well as an increase in the grain size, and the improvement in crystal structure of AZO with increasing deposition temperature. The better crystallinity of the films should result in a reduction of scattering centers for electrons, and thus an increase in carrier mobility. At substrate temperatures above 250 °C, the ENZ wavelength (as well as loss) increases apparently because of inferior crystal quality of AZO the caused by the desorption of precursors at the high temperatures during the deposition process. Figure 8b,e shows that as the Al content increases (dopant ratio ZnO:Al decreases), the ENZ wavelength (as well as loss) first decreases and then increases again. Gurung et al. [96] explained this finding by doping saturation as well as the formation of Zn vacancies at high Al concentrations. As the Al content of AZO increases, the carrier concentration increases until it reaches a maximum value. Incorporation of more Al species leads to their clustering, which gives rise to a decrease in both carrier concentration and mobility. The film thickness also has an effect on the ENZ wavelength, as shown in Figure 8c,f. The longer ENZ wavelengths for the thinner films have been attributed to lower free carrier concentrations in these layers, as 4-5 monolayers of ZnO deposition is required to achieve fully activated Al dopants. [104] With increasing thickness, the ENZ wavelength blueshifts and reaches the value corresponding to the selected dopant ratio. Another factor possibly contributing to the observed blueshift is the increase in the grain size with increasing film thickness.^[96]

Riley et al.^[101] observed a blueshift in the crossover wavelength when a 112 nm ZnO buffer layer between AZO and a silicon substrate was inserted. As the buffer thickness increases from 0 to 112 nm, the wavelength shifted from 1550 to 1450 nm and losses decreased from 0.53 to 0.46 at 1550 nm. This improvement was

explained by better crystallinity of AZO grown on a ZnO buffer layer. The grains in the ZnO films become larger with increasing thickness, therefore, the AZO layers deposited on thicker buffer layers have larger grain sizes and fewer grain boundaries, acting as traps and barriers for free carriers. As a result, the large-grain AZO films showed better conductivity and improved optical properties. Although this result is sound and logical, the use of relatively thick ZnO buffer is not feasible for many modulator applications, where AZO is required to be in direct contact or in close vicinity to Si waveguide.

To obtain ENZ properties covering the entire telecommunication wavelength range (1260-1625 nm) or provide access to biological transparency windows (600-1350 nm), AZO layers with low losses and very high carrier concentration are required. Unfortunately, the ALD-grown AZO often exhibit poor optical quality and insufficient carrier concentrations due to low doping efficiencies at high doping levels (>10²⁰ cm⁻³). [96,101,103] For example, about 60% of Al atoms in AZO layers deposited by reactive magnetron sputtering^[86] and over 90% of Al atoms in CVDgrown AZO^[92] were found to be electrically active, while only about 13% Al worked as dopants in the ALD-grown AZO films. [103] The poor doping efficiency (the ratio of electron concentration to total Al content in the matrix) is a serious limitation of ALD, which results in lower quality of ALD-grown AZO and GZO films compared with those grown by the other methods. This limitation is related to the digital nature of the ALD process. MBE, PLD, CVD, and sputtering techniques involve concurrent delivery of Zn and Al species with precisely controlled flux ratios within a very wide range which gives rise to uniform Al or Ga distribution through the matrix and high doping efficiency. To the contrary, ALD deposition of homogeneous Al-doped ZnO layer is challenging, because simultaneous delivery of Al and Zn species to the substrate results in predominantly Al₂O₃ growth due to the higher adsorption energy of the most widely used Al precursor, (TMA) (or triethylgallium (TEG) in the case of GZO) compared to the Zn precursor (DEZ) on OH⁻ terminated surfaces. [105,106] For this reason, the conventional ALD route for deposition of AZO films consists of two alternating steps: 1) zinc and oxygen precursor alternating pulses for ZnO growth followed by 2) a doping cycle of aluminum and oxygen precursor alternating pulses, which obviously results in the formation of AlO_x/ZnO layered structure. [95,96,103]

To address the doping inefficiency problem, DEZ-TMA-H₂O pulse sequence instead of the TMA-H2O alternating pulses for the doping cycle was proposed. [94,98,102] Fomra et al. [94] used this modified approach to the ALD growth of AZO thin films on silicon and sapphire at substrate temperatures ranging from 200 to 400 °C. As shown in Figure 9, each supercycle consisted of M alternating pulses of DEZ and H₂O, followed by a doping cycle of H₂O, DEZ, and TMA. The overall number of supercycles N was varied to control the film thickness and number M was varied to control the doping concentration. While only Al—O bonds are formed during the conventional doping pulse sequence, the modified pulse sequence promotes competition between Zn-O and Al—O bonds during a doping cycle. The introduction of DEZ into the reaction chamber preceding TMA leads to the formation of Zn-OH bonds, but as the adsorption energy of TMA-OH is larger than that of DEZ-OH, TMA is capable of randomly replacing adsorbed DEZ.[105,106] This decreases the amount of Al



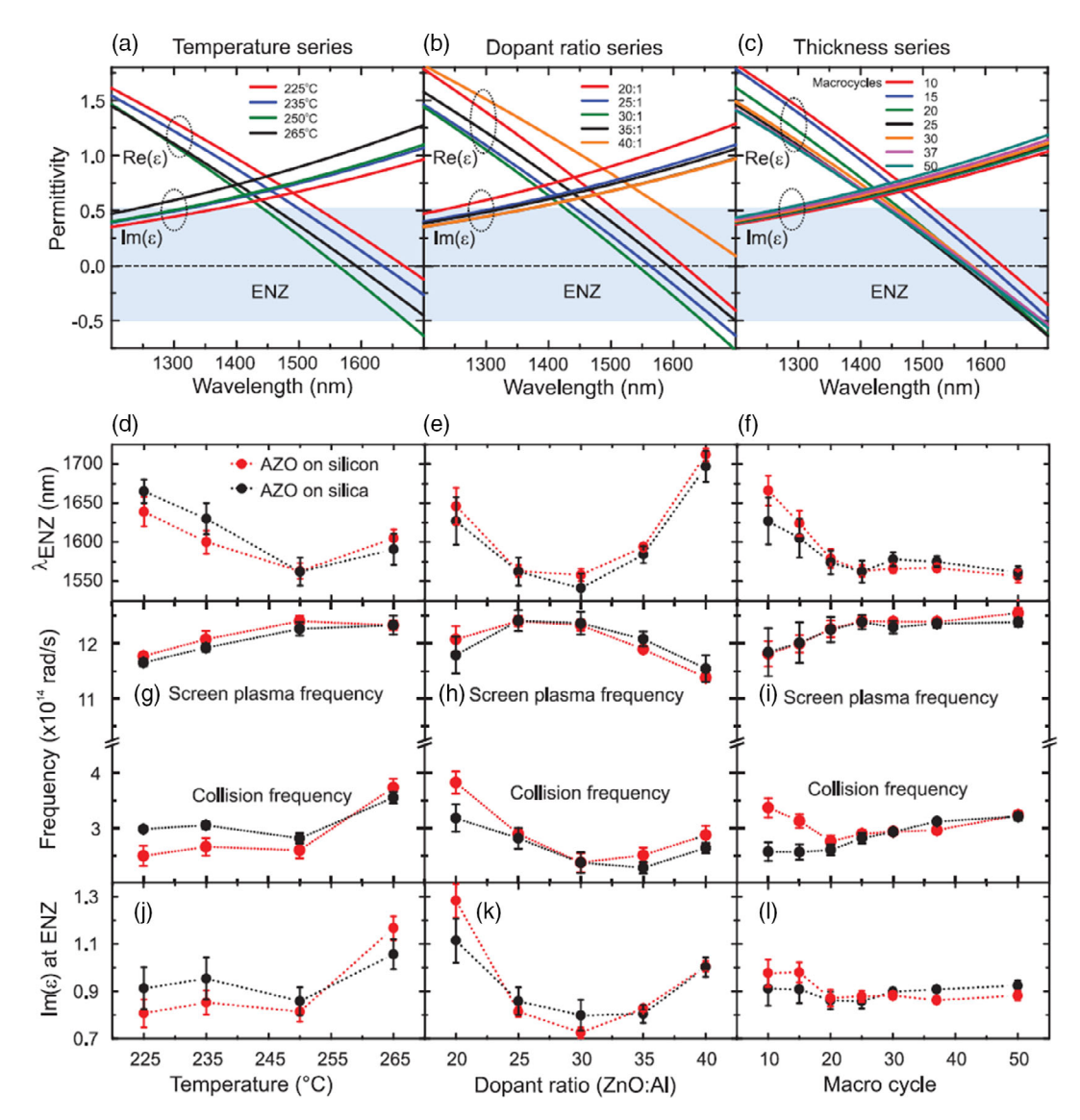


Figure 8. a-c) Wavelength dependences of the real (ϵ') and imaginary (ϵ'') part of permittivity of AZO nanolayers on silica substrates on different ALD parameters: deposition temperature, dopant ratio (ZnO:Al), and the number of macrocycles (thickness). Note that the decrease in dopant ratio indicates more layers of Al dopant in the AZO thin films (i.e., increase in Al content). d-f) Dependences of the ENZ wavelength, g-i) the screened plasma and collision frequencies, and j-l) the imaginary part of the permittivity at ENZ wavelength on different ALD parameters. For the temperature dependence, AZO layers were deposited at a 25:1 dopant ratio; for the dopant ratio dependence, AZO layers were deposited with a dopant ratio of 25:1 at a temperature of 250 °C. The red and black circles represent data points with AZO on silicon and silica, respectively. a-l) Reproduced with permission. [96] Copyright 2020, Wiley-VCH.

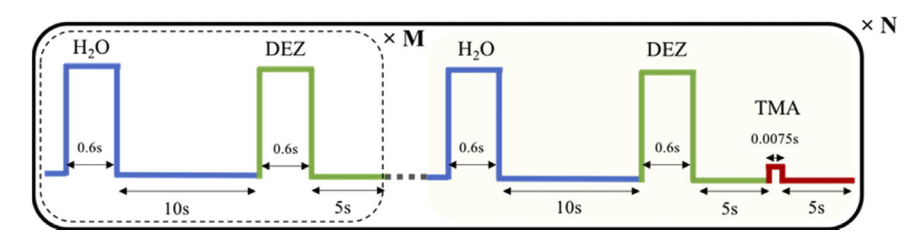


Figure 9. Schematic of the pulse sequence in the modified ALD process. M alternating pulses of H_2O and DEZ are followed by a doping cycle of H_2O , DEZ, and TMA pulses. The frequency of the doping cycle determines the carrier concentration and N number of supercycles determines the thickness. Reproduced with permission.^[94] Copyright 2020, Optical Society of America.



species incorporated into the film, as the active sites are now shared between Al and Zn atoms. To avoid the surface saturation during the TMA pulse, the pulse duration was reduced down to 7.5 ms, which was the minimum reliable switching time of the ALD valve used in a Fiji 2 ALD system (Veeco, Inc.). To further reduce the amount of Al supplied per a pulse, a 100 µm diameter orifice was installed on the head of the TMA precursor bottle. The basic idea was to move away from the surface saturation conditions for the Al precursor pulse, which led to a reduced Al incorporation in each dosing cycle in favor of more frequent pulses. In addition, the increase in substrate temperature to 400 °C allowed decreasing the density of OH⁻ groups on the surface, which act as active sites for Zn⁺ and Al⁺ ions. At increased temperatures, the OH⁻ groups recombine to release H₂O and form O* radicals, the number of active sites decreases, thereby reducing the amount of Al atoms incorporated into the film. Under these conditions, the TMA adsorption was reduced, and the ALD was believed to be operating in a subsaturation regime. The decrease in the active site density resulted also in decreasing growth rate with increasing substrate temperature, from $\approx 0.19 \, \text{nm/cycle}$ at 200 °C to \approx 0.09 nm/cycle at 400 °C. The reduced growth rate not only led to fewer Al ions being incorporated into the matrix during each dosing cycle, but also made it possible to achieve more spatially frequent occurrence of the dopant layers. For example, the dopant layer occurred after every 1 nm of ZnO growth at 200 °C, whereas it occurred after every 0.5 nm of the ZnO growth at 350 °C albeit with a reduced number of Al species incorporated in each layer.

Figure 10 shows temperature dependences of the electrical properties of AZO films deposited on sapphire substrates via the modified ALD procedure. As the substrate temperature increased from 200 to 350 °C, the resistivity dropped from 8×10^{-4} to 4×10^{-4} Ω cm (Figure 10a). The decrease in resistivity was predominantly the result of an increase in carrier mobility (Figure 10b), as the carrier concentration remained approximately constant (Figure 10c). This finding suggests a reduction in clustering of Al species, which decreases the density of scattering centers, thus paving the way to an increase in carrier mobility. The increase in resistivity at substrate temperatures above 350 °C is attributed to an increase in the decomposition

of DEZ and TMA, known to occur at temperatures above 325 °C, which leads to excessive impurity (carbon) incorporation. [107] XPS analysis augmenting the Hall effect measurements revealed the doping efficiency of 54%, [94] which was a great improvement as compared to the doping efficiency of 13% reported for the conventional ALD process. [103] It should be noted that even better control over Al incorporation into the ZnO lattice can be achieved, if one will use a smaller orifice and/or a faster ALD valve controlling TMA delivery. This would make it possible to reduce the amount of Al incorporated into the growing ZnO matrix per pulse and use more frequent TMA pulses. We anticipate that these hardware and process modifications will further improve the uniformity of Al distribution in the AZO lattice as well as its activation efficiency. However, it has to be experimentally confirmed yet.

The highest carrier concentration of almost $8 \times 10^{20} \, \text{cm}^{-3}$ has been achieved for an Al dosing percentage (ratio of H₂O/DEZ/ TMA pulses to H₂O/DEZ pulses) of 20%, which in turn resulted in an ENZ wavelength of less than 1400 nm for both sapphire and silicon substrates, as shown in Figure 11 representing ENZ wavelength as a function of Al dosing for 45 nm-thick films. Increasing the dosing percentage further caused a decrease in free carrier concentration, presumably due to the formation of alumina inclusions. Although Hall mobility decreased gradually from 32 to 20 cm² V s⁻¹ when the dosing percentage increased from 2% to 20%, the optical losses remained sufficiently low (0.55 on sapphire and 0.45 on silicon). Moreover, thus grown 100 nm-films films exhibit ENZ wavelengths as short as 1320 and 1370 nm for sapphire and Si substrates, respectively, and a resistivity of $2.8 \times 10^{-4} \Omega$ cm.^[94] Note that this value is comparable with the resistivity of $2.4\times 10^{-4}\,\Omega$ cm reported for thick (700–900 nm) sputtered films.^[108] The losses of these films $(\varepsilon'' = 0.35)^{[94]}$ are approaching and in certain cases even outperforming that of PLD $(\varepsilon'' = 0.26)^{[83]}$ and sputtered films $(\varepsilon'' \approx 0.7)$, [42] while offering better thickness control, which is advantageous for nanophotonic devices that typically require the use of sub-50 nm thin films. To summarize, the AZO produced through the modified ALD process provides tunability of crossover wavelength from 1320 to 1625 nm, thus covering most of telecommunication range, and even extending into the edge of the

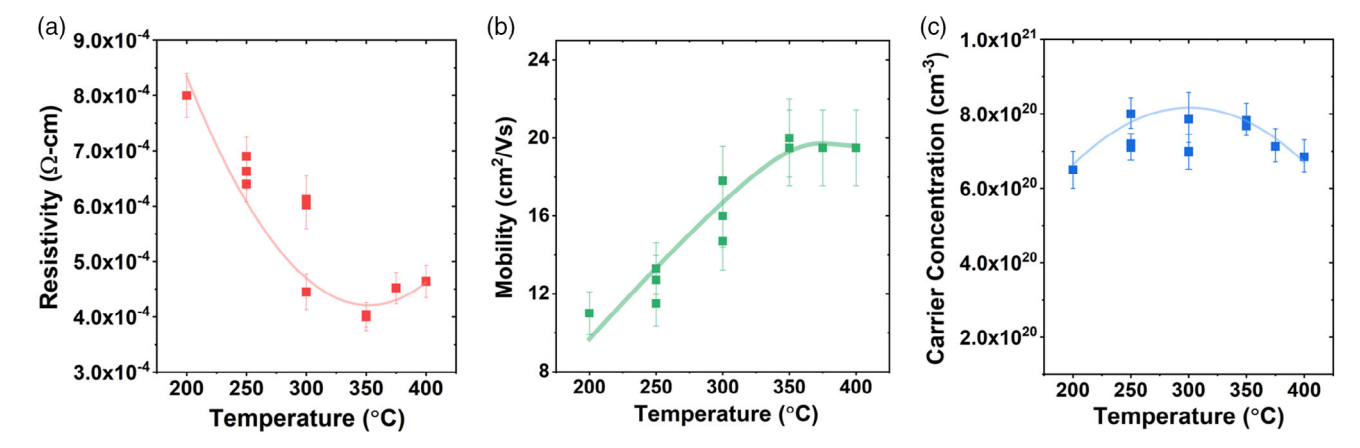


Figure 10. a–c) Substrate temperature dependences of the resistivity (a), Hall mobility (b), and carrier concentration (c) of 45 nm-thick AZO films deposited on sapphire substrates at 20% Al dosing percentage (ratio of H₂O/DEZ/TMA pulses to H₂O/DEZ pulses). a–c) Adapted with permission.^[94] Copyright 2020, Optical Society of America.





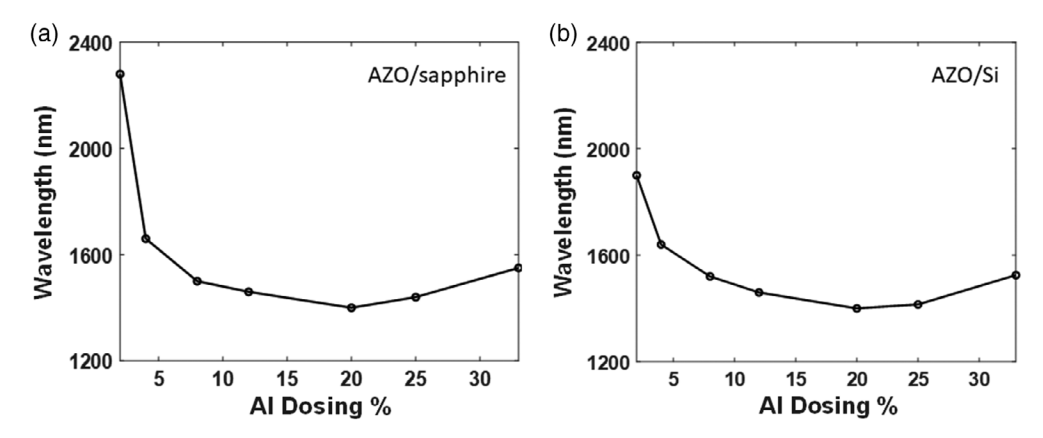


Figure 11. a,b) ENZ wavelength versus Al dosing for 45 nm-thick AZO films on sapphire (a) and Si (b) substrates grown by ALD under the optimized conditions (substrate temperature 350 $^{\circ}$ C, 7.5 ms TMA pulse duration (with orifice), and H₂O/DEZ/TMA dosing sequence).

biological transparency window while maintaining low optical losses: crossover wavelengths as low as 1320 nm on sapphire and 1370 nm on silicon with losses of 0.45 and 0.35, respectively. The short crossover wavelength coupled with low losses, reinforced by the advantages of the ALD method, makes the ALD-grown films extremely attractive for a range of dynamic nanophotonic metadevices. **Table 2** shows the comparison of published data on electronic and plasmonic properties of AZO films deposited by ALD and other techniques on different substrates.

4. Conclusion and Outlook

By coupling electromagnetic radiation to collective oscillations of free electrons, plasmonics provides a way to manipulate light at scales smaller than the diffraction limit and drastically enhance light–matter interaction, which has enabled the emergence of novel technologies with combined capabilities of photonics and microelectronics. Combining plasmonics with traditional Si electronics requires the development of deposition techniques compatible with the CMOS process. The deposition technique of choice should provide high plasmonic quality of materials (evaluated through plasmonic FoM = $-\epsilon''/\epsilon''$) while keeping the deposition temperature sufficiently low (<550 °C) to retain the integrity of Si-based CMOS circuitry. ALD which offers excellent conformity and scalability in addition to low growth temperature seems to be a natural choice for CMOS compatible plasmonics. One should note that the development of deposition methods for high-K dielectrics (principally, HfO₂) for CMOS electronics was a major driving force for advances in the ALD techniques.

Table 2. Deposition technique, deposition temperature T_S , thickness t, resistivity ρ , free electron concentration n, epsilon-near-zero wavelength λ_{ENZ} , losses ε'' at λ_{ENZ} , and mobility μ for AZO films on various substrates.

Film/substrate	Method ^{a)}	$T_S [^{\circ}C]^{a)}$	t [nm]	$ ho \; [\Omega { m cm}]$	$n [\text{cm}^{-3}]$	λ_{ENZ} [nm]	ε'' at λ_{ENZ}	$\mu \text{ [cm}^2 \text{ V}^{-1} \text{ s}^{-1} \text{]}$	Ref.
AZO/sapphire	ALD	350	100	2.8×10^{-4}	8.6×10^{20}	1320	0.45	26	[94]
AZO/Si		350	100	-	-	1370	0.35	-	
AZO/silica	ALD	250	53.8	4.6×10^{-4}	6.5×10^{20}	1497	≈0.68	21	[95]
AZO/glass	ALD	_	577	7.9×10^{-4}	>10 ²⁰	1570	0.5	-	[99]
AZO/silica	ALD	250	65	-	_	1500	0.77	-	[96]
AZO/Si	ALD	250 + PDA at 825	56	3.8×10^{-4}	1.5×10^{21}	1545	0.53	9.8	[101]
AZO/ZnO/Si			56	-	_	1450	0.38		
AZO/glass	ALD	150	90	5.7×10^{-4}	2.2×10^{21}	-	_	4.6	[98]
AZO/SiO ₂ /Si	ALD	200	41–45	32×10^{-4}	1.4×10^{20}	-	_	14.3	[103]
AZO/fused silica	PLD	RT	350	-	9.8×10^{20}	1300	0.26	-	[83]
AZO/glass	Reactive MS	300	793	2.4×10^{-4}	6.8×10^{20}	-	_	38	[108]
AZO/Si	RF MS	RT + PDA at 250	300	_	_	1375	0.69	-	[42]
AZO/SiN/glass	RF MS	300 + PDA at 650	_	1.35×10^{-4}	6.9×10^{20}	_	_	67	[85]
AZO/soda lime glass	CVD	420	790	3.0×10^{-4}	8.8×10^{20}	-	_	23.3	[92]
AZO	Photo-MOCVD	140	1400	6.22×10^{-4}	5×10^{20}	-	_	≈22	[93]

^{a)}The following abbreviations are used in the table: atomic layer deposition (ALD), pulsed laser deposition (PLD), radio frequency (RF), magnetron sputtering (MS), chemical vapor deposition (CVD), photo-assisted metal-organic chemical vapor deposition (photo-MOCVD), post-deposition annealing (PDA), room temperature (RT).





gallium oxide, etc., which are attracting a great interest due to their large nonlinearities at telecommunication wavelengths near the ENZ region.

However, until recently, TiN fabricated by plasma-enhanced ALD has suffered from low FoM values and high loss compared with the material prepared by other methods such as sputtering, PLD, and MBE. The major obstacles were contaminations (mainly oxygen and carbon) and low structural quality. The considerable reduction in the level of chemical contaminations has been recently achieved via the usage of sapphire plasma sources and extended plasma exposure times, whereas the structural quality of TiN has been improved by decreasing the chemisorption time of Ti-precursor TDMAT and increasing the deposition temperature within the CMOS compatible range (to 450° C).

Toward the CMOS compatible process, the employment of MgO buffer layer on Si has been shown to result in the material quality on par with that of TiN grown on bulk MgO, the bestknown substrate material for achieving high-quality TiN. Recently reported plasmonic FoM of ALD-grown TiN (FoM = 2.8) is approaching that for the material prepared by the higher temperature deposition techniques, e.g., sputtering and PLD. This progress led to the demonstration of ALD-grown TiN-based metasurfaces exhibiting plasmonic colors. One can expect that even better TiN films can be grown by ALD if the material purity would be improved further and deposition temperature would be increased to 475-500 °C. The former can be accomplished using reactors dedicated to the nitride growth and oxygen-free plasma source (e.g., BN plasma tube), while the increase in the deposition temperature requires a Ti precursor with higher decomposition temperature than that of popular TDMAT, e.g., TDEAT.

Considerable progress has also been made recently in ALD deposition of TCO materials, primarily Al-doped ZnO (AZO), which are attracting a great deal of attention as an ENZ material for the telecommunication wavelength. The major "show stopper" in the AZO case is the low efficiency of Al activation caused by the digital nature of the ALD process which facilitates Al clustering and formation of aluminum oxide instead of substituting Zn on lattice sites. Modification of the pulse sequence (the use of DEZ-TMA-H₂O pulse sequence instead of the TMA-H₂O alternating pulses for the doping cycle) together with reducing TMA pulse duration allowed better doping control through reduced adsorption of Al species in each dosing cycle, more uniform Al distribution in the growth direction, and reduced clustering alumina inclusions formed from excessive Al species. This gave rise to the improved activation efficiency which was estimated to increase from some 15% to 54%. Consequently, the carrier concentration in the material grown at the optimized temperature of 375 °C was 8×10^{20} cm⁻³, which made it possible to tune the ENZ frequency from 1320 to 1665 nm, thus covering most of the telecommunication range. The loss in these films $(\varepsilon'' = 0.35)$ has been noted to approach, and in certain cases even outperform, the loss level achieved for PLD ($\varepsilon'' = 0.26$) and sputtered ($\varepsilon'' \approx 0.7$) AZO.

Reduction of the purge time for TMA, DEZ, and $\rm H_2O$ for processes with substrate temperature of around 350 °C, which is slightly above the decomposition temperatures of Al and Zn precursors, can improve the structural quality of the material, thus addressing not only doping efficiency but also the loss. Moreover, the modified ALD process opens an avenue toward improving the plasmonic performance of other doped oxide and nitride semiconductors, such as gallium nitride, cadmium oxide,

Acknowledgements

This work was partially funded by the Virginia Commonwealth Cyber Initiative, NSF grant 1808928, and AFOSR grant FA9550-1-18-0151.

Conflict of Interest

The authors declare no conflict of interest.

Keywords

Al-doped ZnO, atomic layer deposition, epsilon-near-zero materials, nanophotonics, plasmonic materials, TiN, ZnO

Received: April 26, 2021 Revised: June 13, 2021 Published online:

- S. A. Maier, M. L. Brongersma, P. G. Kik, S. Meltzer, A. A. G. Requicha, H. A. Atwater, Adv. Mater. 2001, 13, 1501.
- [2] D. K. Gramotnev, S. I. Bozhevolnyi, Nat. Photonics 2010, 4, 83.
- [3] J. A. Dionne, Nat. Mater. 2013, 12, 380.
- [4] S. A. Maier, Plasmonics: Fundamentals and applications, Springer, New York 2007.
- [5] B. Dastmalchi, P. Tassin, T. Koschny, C. Soukoulis, Adv. Opt. Mater. 2016, 4, 177.
- [6] N. Kinsey, C. DeVault, A. Boltasseva, V. M. Shalaev, Nat. Mater. 2019, 4, 742
- [7] X. Han, K. Liu, C. Sun, Plasmonics Biosens. Mater. 2019, 12, 1411.
- [8] M. Mesch, B. Metzger, M. Hentschel, H. Giessen, Nano Lett. 2016, 16, 3155
- [9] A. G. Brolo, Nature Photonics 2012, 6, 709.
- [10] N. S. Abadeer, C. J. Murphy, J. Phys. Chem. C 2016, 120, 4691.
- [11] L. R. Hirsch, R. J. Stafford, J. A. Bankson, S. R. Sershen, B. Rivera, R. E. Price, J. D. Hazle, N. J. Halas, J. L. West, PNAS 2003, 100, 13549.
- [12] W. Cai, A. Vasudev, M. Brngersma, Science 2006, 311, 1901.
- [13] M. S. Tame, K. R. McEnery, Ş. K. Özdemir, J. Lee, S. A. Maier, M. S. Kim, Nat. Phys. 2013, 9, 329.
- [14] M. Kauranen, A. V. Zayats, Nat. Photonics 2012, 6, 737.
- [15] P. Wang, M. E. Nasir, A. V. Krasavin, W. Dickson, Y. Jiang, A. V. Zayats, Acc. Chem. Res. 2019, 52, 3018.
- [16] K. Yang, J. Wang, X. Yao, D. Lyu, J. Zhu, Z. Yang, B. Liu, B. Ren, Adv. Opt. Mater. 2021, 9, 2001375.
- [17] J. C. Ndukaife, A. V. Kildishev, A. G. A. Nnanna, V. M. Shalaev, S. T. Wereley, A. Boltasseva, Nat. Nanotechnol. 2016, 11, 53.
- [18] K. R. Catchpole, A. Polman, Opt. Express 2008, 16, 21793.
- [19] S. V. Boriskina, H. Ghasemi, G. Chen, Mater. Today, 2013, 16, 375.
- [20] N. Kinsey, M. Ferrera, V. Shalaev, A. Boltasseva, J. Opt. Soc. Am. B 2015, 32, 121.
- [21] C. Haffner, D. Chelladurai, Y. Fedoryshyn, A. Josten, B. Baeuerle, W. Heni, T. Watanabe, T. Cui, B. Cheng, S. Saha, D. L. Elder, L. R. Dalton, A. Boltasseva, V. M. Shalaev, N. Kinsey, J. Leuthold, *Nature* 2018, 556, 483.
- [22] W. O. F. Carvalho, J. Rm Mejía-Salazar, Sensors 2020, 20, 2488.
- [23] Z. Ullah, G. Witjaksono, I. Nawi, N. Tansu, M. I. Khattak, M. Junaid, Sensors 2020, 20, 1401.





- [24] G. Lozano, D. J. Louwers, S. R. Rodríguez, S. Murai, O. T. Jansen, M. A. Verschuuren, J. G. Rivas, Light: Sci. Applic. 2013, 2, e66.
- [25] R. F. Oulton, V. J. Sorger, T. Zentgraf, R.-M. Ma, C. Gladden, L. Dai, G. Bartal, X. Zhang, *Nature* 2009, 461, 629.
- [26] M. B. Cortie, M. D. Arnold, V. J. Keast, Adv. Mater. 2020, 32, 1904532.
- [27] P. Berini, Opt. Express 2006, 14, 13030.
- [28] G. V. Naik, V. M. Shalaev, A. Boltasseva, Adv. Mater. 2013, 25, 3264.
- [29] P. R. West, S. Ishii, G. V. Naik, N. K. Emani, V. M. Shalaev, A. Boltasseva, Laser Photon. Rev. 2010, 4, 795.
- [30] G. Naik, J. Kim, A. Boltasseva, Opt. Mater. Express 2011, 1, 1090.
- [31] P. Patsalas, N. Kalfagiannis, S. Kassavetis, G. Abadias, D. V. Bellas, C. Lekka, E. Lidorikis, *Mater. Sci. Eng. R* 2018, 123, 1.
- [32] J. Fan, M. Sun, Chem. Rec. 2020, 20, 1043.
- [33] P. A. D. Goncalves, N. Stenger, J. D. Cox, N. A. Mortensen, S. Xiao, Adv. Opt. Mater. 2020, 8, 1901473.
- [34] S. A. Maier, Nat. Phys. 2012, 8, 581.
- [35] K. S. Novoselov, A. Mishchenko, A. Carvalho, A. H. C. Neto, *Science* 2016, 353, 9439.
- [36] H. Liu, A. T. Neal, Z. Zhu, Z. Luo, X. F. Xu, D. Tomanek, P. D. Ye, ACS Nano 2014, 8, 4033.
- [37] M. N. Gadalla, A. S. Greenspon, M. Tamagnone, F. Capasso, E. L. Hu, ACS Appl. Nano Mater. 2019, 2, 3444.
- [38] W.-P. Guo, R. Mishra, C.-W. Cheng, B.-H. Wu, L.-J. Chen, M.-T. Lin, S. Gwo, ACS Photonics 2019, 6, 1848.
- [39] G. Naik, J. Schroeder, X. Ni, A. Kildishev, T. Sands, A. Boltasseva, Opt. Mater. Express 2012, 2, 478.
- [40] A. Catellani, A. Calzolari, Phys. Rev. B: Condens. Matter Mater. Phys. 2017, 95, 115145.
- [41] I.-S. Yu, H.-E. Cheng, C.-C. Chang, Y.-W. Lin, H.-T. Chen, Y.-C. Wang, Z.-P. Yang, Opt. Mater. Express 2017, 7, 777.
- [42] Y. Wang, A. Capretti, L. Dal Negro, Opt. Mater. Express 2015, 5, 2415.
- [43] R. P. Sugavaneshwar, S. Ishii, T. D. Dao, A. Ohi, T. Nabatame, T. Nagao, ACS Photonics 2018, 5, 814.
- [44] G. V. Naik, B. Saha, J. Liu, S. M. Saber, E. A. Stach, J. M. Irudayaraj, T. D. Sands, V. M. Shalaev, A. Boltasseva, *Proc. Natl. Acad. Sci. USA* 2014, 111, 7546.
- [45] H. Reddy, U. Guler, Z. Kudyshev, A. V. Kildishev, V. M. Shalaev, A. Boltasseva, ACS Photonics 2017, 4, 1413.
- [46] C. M. Zgrabik, Doctoral dissertation, Harvard University, 2016.
- [47] K. Ding, D. Fomra, A. V. Kvit, N. Kinsey, Ü. Özgür, H. Morkoç, V. Avrutin, Adv. Photonics Res., https://doi.org/10.1002/adpr. 202000210.
- [48] N. Kinsey, M. Ferrera, G. V. Naik, V. Babicheva, V. M. Shalaev, A. Boltasseva, Opt. Express 2014, 22, 12238.
- [49] J. Hu, X. Ren, A. N. Reed, T. Reese, D. Rhee, B. Howe, L. J. Lauhon, A. M. Urbas, T. W. Odom, ACS Photonics 2017, 4, 606.
- [50] L. Gui, S. Bagheri, N. Strohfeldt, M. Hentschel, C. M. Zgrabik, B. Metzger, H. Linnenbank, E. L. Hu, H. Giessen, *Nano Lett.* 2016, 16, 5708.
- [51] J. A. Briggs, G. V. Naik, T. A. Petach, B. K. Baum, D. Goldhaber-Gordon, J. A. Dionne, Appl. Phys. Lett. 2016, 108, 051110.
- [52] W. He, K. Ai, C. Jiang, Y. Li, X. Song, L. Lu, *Biomaterials* **2017**, *37*, 132.
- [53] D. Shah, H. Reddy, N. Kinsey, V. M. Shalaev, A. Boltasseva, Adv. Opt. Mater. 2017, 5, 1700065.
- [54] C. M. Zgrabik, E. L. Hu, Opt. Mater. Express 2015, 5, 2786.
- [55] S. Murai, K. Fujita, Y. Daido, R. Yasuhara, R. Kamakura, K. Tanaka, Opt. Express 2016, 24, 1143.
- [56] K. C. Maurya, V. M. Shalaev, A. Boltasseva, B. Saha, Opt. Mater. Express 2020, 10, 2679.
- [57] D. Fomra, R. Secondo, K. Ding, V. Avrutin, N. Izyumskaya, Ü. Özgür, N. Kinsey, J. Appl. Phys. 2020, 127, 103101.
- [58] E. Langereis, S. B. S. Heil, M. C. M. van de Sanden, W. M. M. Kessels, J. Appl. Phys. 2006, 100, 023534.

- [59] L. M. Otto, A. T. Hammack, S. Aloni, D. F. Ogletree, D. L. Olynick, S. Dhuey, B. J. H. Stadler, A. M. Schwartzberg, *Proc. SPIE* 2020, 9919, 99190N.
- [60] K. Hansen, M. Cardona, A. Dutta, C. Yang, Materials 2020, 13, 1058.
- [61] G. B. Rayner Jr., N. O'Toole, J. Shallenberger, B. Johs, J. Vac. Sci. Technol. A 2020, 38, 062408.
- [62] I. Krylov, X. Xu, K. Weinfeld, V. Korchnoy, D. Ritter, M. Eizenberg, J. Vac. Sci. Technol. A 2019, 37, 010906.
- [63] I. Krylov, V. Korchnoy, X. Xu, K. Weinfeld, E. Yalon, D. Ritter, M. Eizenberg, J. Appl. Phys. 2020, 128, 065301.
- [64] B. Kim, N. Lee, J. Lee, T. Park, H. Park, Y. Kim, C. Jin, D. Lee, H. Kim, H. Jeon, Appl. Surf. Sci. 2021, 541, 148482.
- [65] S. Belahcen, C. Vallée, A. Bsiesy, A. Chaker, M. Jaffal, T. Yeghoyan, M. Bonvalot, J. Vac. Sci. Technol. A 2021, 39, 012410.
- [66] I. Krylov, Y. Qi, V. Korchnoy, K. Weinfeld, M. Eizenberg, E. Yalon, J. Vac. Sci. Technol. A 2020, 38, 032403.
- [67] H. Van Bui, A. Y. Kovalgin, R. A. M. Wolters, Appl. Surf. Sci. 2013, 269, 45
- [68] E. Langereis, S. B. S. Heil, H. C. M. Knoops, W. Keuning, M. C. M. van de Sanden, W. M. M. Kessels, J. Phys. D: Appl. Phys. 2009, 42, 073001.
- [69] H. C. M. Knoops, T. Faraz, K. Arts, W. M. M. Kessels, J. Vac. Sci. Technol. A 2019, 37, 030902.
- [70] J. P. A. M. Driessen, J. Schoonman, K. F. Jensen, J. Electrochem. Soc. 2001, 148, G178.
- [71] C.-C. Chang, J. Nogan, Z.-P. Yang, W. J. Kort-Kamp, W. Ross, T. S. Luk, D. A. Dalvit, A. K. Azad, H.-T. Chen, Sci. Rep. 2019, 9, 15287.
- [72] J. Narayan, P. Tiwari, X. Chen, J. Singh, R. Chowdhury, T. Zheleva, Appl. Phys. Lett. 1992, 61, 1290.
- [73] I. Krylov, X. Xu, Y. Qi, K. Weinfeld, V. Korchnoy, M. Eizenberg, D. Ritter, J. Vac. Sci. Technol. A 2019, 37, 060905.
- [74] K. Ding, D. Fomra, V. Avrutin, N. Kinsey, Ü. Özgür, H. Morkoç, in Frontiers in Optics + Laser Science APS/DLS, OSA Technical Digest, 2019, paper JW3A.71.
- [75] J. Pelleg, L. Zevin, S. Lungo, N. Croitoru, *Thin Solid Films* **1991**, *197*,
- [76] S. Vangelista, R. Mantovan, A. Lamperti, G. Tallarida, B. Kutrzeba-Kotowska, S. Spiga, M. Fanciulli, J. Phys. D: Appl. Phys. 2013, 46, 485304.
- [77] D. Fomra, Md. Mamun, K. Ding, V. Avrutin, Ü. Özgür, N. Kinsey, *Opt. Express* 2021, 29, 19586.
- [78] A. P. Vinogradov, A. V. Dorofeenko, I. A. Nechepurenko, Metamaterials 2010, 4, 181.
- [79] H. F. Ghaemi, T. Thio, D. E. Grupp, T. W. Ebbesen, H. J. Lezec, *Phys. Rev. B* 1998, 58, 6779.
- [80] C. Genet, T. W. Ebbesen, Nature 2007, 445, 39.
- [81] N. Kinsey, M. Ferrera, G. V. Naik, V. E. Babicheva, V. M. Shalaev, A. Boltasseva, Opt. Express 2014, 22, 12238.
- [82] G. V. Naik, A. Boltasseva, Metamaterials 2011, 5, 1.
- [83] N. Kinsey, C. DeVault, J. Kim, M. Ferrera, V. M. Shalaev, A. Boltasseva, Optica 2015, 2, 616.
- [84] Ü. Özgür, Y. I. Alivov, C. Liu, A. Teke, M. A. Reshchikov, S. Dŏgan, V. Avrutin, S. J. Cho, H. Morkoç, J. Appl. Phys. 2005, 98, 041301.
- [85] F. Ruske, M. Roczen, K. Lee, M. Wimmer, S. Gall, J. Hüpkes, D. Hrunski, B. Rech, J. Appl. Phys. 2010, 107, 013708.
- [86] K. Ellmer, F. Kudella, R. Mientus, R. Schieck, S. Fiechter, Thin Solid Films 1994, 247, 15.
- [87] A. V. Kvit, A. B. Yankovich, V. Avrutin, H. Liu, N. Izyumskaya, Ü Özgür, H. Morkoç, P. M. Voyles, J. Appl. Phys. 2012, 112, 123527.
- [88] H. Y. Liu, V. Avrutin, N. Izyumskaya, Ü. Özgür, A. B. Yankovich, A. V. Kvit, P. M. Voyles, H. Morkoc, J. Appl. Phys. 2012, 111, 103713.
- [89] S. Kalusniak, S. Sadofev, F. Henneberger, Phys. Rev. Lett. 2014, 112, 137401





- [90] V. Bhosle, J. T. Prater, F. Yang, D. Burk, S. R. Forrest, J. Narayan, J. Appl. Phys. 2007, 102, 023501.
- [91] H. Agura, A. Suzuki, T. Matsushita, T. Aoki, M. Okuda, *Thin Solid Films* 2003, 445, 263.
- [92] J. Hu, R. G. Gordon, J. Appl. Phys. 1992, 71, 880.
- [93] S. Y. Myong, S. J. Baik, C. H. Lee, W. Y. Cho, K. S. Lim, Jpn. J. Appl. Phys. 1997, 36, 1078.
- [94] D. Fomra, K. Ding, V. Avrutin, Ü. Özgür, N. Kinsey, Opt. Mater. Express 2020, 10, 3060.
- [95] A. Anopchenko, S. Gurung, L. Tao, C. Arndt, H. W. H. Lee, *Mater. Res. Express* 2018, 5, 014012.
- [96] S. Gurung, A. Anopchenko, S. Bej, J. Joyner, J. D. Myers, J. Frantz, H. W. H. Lee, Adv. Mater. Interfaces 2020, 7, 2000844.
- [97] E. Shkondin, O. Takayama, M. E. A. Panah, P. Liu, P. V. Larsen, M. D. Mar, F. Jensen, A. V. Lavrinenko, Opt. Mater. Express 2017, 7, 1606.
- [98] Y. Li, R. Yao, H. Wang, X. Wu, J. Wu, X. Wu, W. Qin, ACS Appl. Mater. Interfaces 2017, 9, 11711.

- [99] A. K. Pradhan, R. M. Mundle, K. Santiago, J. R. Skuza, B. Xiao, K. D. Song, M. Bahoura, R. Cheaito, P. E. Hopkins, Sci. Rep. 2015, 4, 6415.
- [100] Y.-L. Lee, T.-H. Huang, C.-L. Ho, M.-C. Wu, ECS J. Solid State Sci. Technol. 2013, 2, Q182.
- [101] C. T. Riley, J. S. T. Smalley, K. W. Post, D. N. Basov, Y. Fainman, D. Wang, Z. Liu, D. J. Sirbuly, *Small* **2016**, *12*, 892.
- [102] J. S. Na, Q. Peng, G. Scarel, G. N. Parsons, Chem. Mater. 2009, 21, 5585.
- [103] D. J. Lee, H. M. Kim, J. Y. Kwon, H. Choi, S. H. Kim, K. B. Kim, Adv. Funct. Mater. 2011, 21, 448.
- [104] J.-S. Na, G. Scarel, G. N. Parsons, J. Phys. Chem. C 2010, 114, 383.
- [105] T. Weckman, K. Laasonen, J. Phys. Chem. C 2016, 120, 21460.
- [106] D. H. Kim, S. Bin Baek, Y. C. Kim, Appl. Surf. Sci. 2011, 258, 225.
- [107] C. Thiandoume, V. Sallet, R. Triboulet, O. Gorochov, J. Cryst. Growth 2009, 311, 1411.
- [108] J. Hüpkes, B. Rech, S. Calnan, O. Kluth, U. Zastrow, H. Siekmann, M. Wuttig, Thin Solid Films 2006, 502, 286.



Natalia Izyumskaya received her Ph.D. degree from the Institute of Microelectronics Technology, Russian Academy of Sciences, in 1999. She held the positions of research scientist at the Institute of Microelectronics Technology, Russia, and later visiting research scientist at University of Ulm, Germany. She joined Department of Electrical and Computer Engineering, Virginia Commonwealth University, in 2005. Her current research interests include epitaxial growth, characterization, and device applications of III-nitrides, ZnO, multifunctional complex oxides, and plasmonic materials.



Dhruv Fomra received his bachelor's degree in nanotechnology from SRM University, India, in 2017. During his undergrad, he completed summer internships at the research labs of 3M India and the Indian Institute of Science at Bangalore. In the fall of 2017, he joined the Ph.D. program in electrical engineering at Virginia Commonwealth University. His current research revolves around development of optical materials and designing transitional integrated photonic technologies to support existing telecommunication systems, such as Tbps modulators and nanoscale optical routers, as well as exploratory work focused on the realization of next-generation computational technologies such as optical neural networks and all-optical systems.



Kai Ding received his Ph.D. degree in material physics and chemistry from the Institute of Semiconductors, Chinese Academy of Sciences, Beijing, China, in 2010. He is currently a research associate with the Department of Electrical and Computer Engineering, Virginia Commonwealth University. He has been involved in growth and processing of III-nitrides and oxide wide-bandgap semiconductors for applications in visible and ultraviolet light-emitting diodes, and heterostructure field-effect transistors. His current research interests include plasmonic materials and nanophotonic devices.



Hadis Morkoç received his Ph.D. degree in electrical engineering from Cornell University, Ithaca, NY, USA. From 1976 to 1978, he was with Varian Associates, Palo Alto, CA, USA. Between 1978 and 1997, he held visiting positions at the AT&T Bell Laboratories, the California Institute of Technology, Pasadena, and Jet Propulsion Laboratory, and the Air Force Research Laboratories-Wright Patterson AFB as a University Resident Research Professor. From 1978 to 1997, he was with the University of Illinois, Urbana. In 1997, he joined as a founder Professor at the newly established School of Engineering at Virginia Commonwealth University, Richmond, VA, USA.







Nate Kinsey received his bachelor's degree in electrical engineering from the University of Missouri—Columbia, in 2011. He followed with his M.Sc. from the University of Missouri, in 2012, where he researched optically activated solid-state switches for high energy RF systems. Following, he moved to Purdue University as a Meissner Fellow to pursue his Ph.D. where he researched nonlinear optics, integrated nanophotonics, and plasmonics. In the fall of 2016, he joined Virginia Commonwealth University as an Assistant Professor of Electrical and Computer Engineering where he has continued his studies of light—matter interactions.



Ümit Özgür received B.S. degrees in electrical engineering and physics from Bogazici University, Istanbul, Turkey, in 1996, and Ph.D. degree in physics from Duke University, in 2003. He was appointed to Qimonda Professor, in 2019. He has published over 250 journal and conference papers and 8 book chapters on growth, fabrication, and characterization of semiconductor materials and devices. He is the coauthor of the book "Zinc Oxide: Fundamentals, Materials and Device Technology" (Wiley, 2009). He is senior member of IEEE, and a member of APS and SPIE.



Vitaliy Avrutin received his Ph.D. degree in physics and mathematics from Institute of Microelectronics Technology, Russian Academy of Sciences, in 1999. He has held the positions of research scientist at Institute of Microelectronics Technology, Russian Academy of Sciences, Chernogolovka, Russia, and later at the Department of Semiconductor Physics, University of Ulm, Germany. Currently, he is Associate Professor in the Electrical and Computer Engineering Department of Virginia Commonwealth University. His research interests encompass growth, characterization and device applications of semiconductor, nanophotonic, and plasmonic materials. He is a member of the American Physical Society, the Materials Research Society, and IEEE.